RESEARCH ARTICLE | OCTOBER 10 2023

Simulation of droplet entrainment in annular flow with a morphology adaptive multifield two-fluid model ⊘

Li-Song Wang (王黎松) ⓘ ; Benjamin Krull ⓘ ; Dirk Lucas ⓘ ; Richard Meller ⓘ ; Fabian Schlegel ✉ ⓘ ;
Matej Tekavčič ⓘ ; Jing-Yu Xu (许晶禹) ✉ ⓘ

Check for updates

View Online   Export Citation

AIP Publishing

Simulation of droplet entrainment in annular flow with a morphology adaptive multifield two-fluid model

View Online   Export Citation   CrossMark

Li-Song Wang (王黎松),[1,2] Benjamin Krull,[3] Dirk Lucas,[3] Richard Meller,[3] Fabian Schlegel,[3,a] Matej Tekavčič,[4] and Jing-Yu Xu (许晶禹)[1,2,a]

AFFILIATIONS

[1]School of Engineering Sciences, University of Chinese Academy of Sciences, No.1 Yanqihu East Road, Beijing 100049, China
[2]Institute of Mechanics, Chinese Academy of Sciences, No.15 Beisihuanxi Road, Beijing 100190, China
[3]Institute of Fluid Dynamics, Helmholtz-Zentrum Dresden - Rossendorf, Bautzner Landstraße 400, Dresden 01328, Germany
[4]Reactor Engineering Division, Jožef Stefan Institute, Jamova cesta 39, Ljubljana 1000, Slovenia

[a]Authors to whom correspondence should be addressed: f.schlegel@hzdr.de and xujingyu@imech.ac.cn

ABSTRACT

Modeling of annular flow with the computational fluid dynamics (CFD) is challenging as one has to consider several, rather different, phenomena simultaneously: the continuous liquid film, continuous gas core, and dispersed droplets. A morphology-adaptive multifield two-fluid model (*MultiMorph*) developed by Meller *et al.* ["Basic verification of a numerical framework applied to a morphology adaptive multi-field two-fluid model considering bubble motions," Int. J. Numer. Methods Fluids 93(3), 748–773 (2021)], with three numerical phase fields, is well suited to simulate such multiple flow structures. Droplet formation plays an important role in annular flow, and a new droplet entrainment model is proposed, expressed as a phase morphology transfer term from the continuous liquid film to dispersed droplets phase field. The new model is developed based on the shear-off entrainment mechanism on the interfacial wave, implying that the droplet formation is dominated by the balance between the shear forces and the surface tension forces at the gas–liquid interface. In contrast to the existing entrainment models, the new model considers the flow parameters locally at the interface, and it is suitable for phase-resolving CFD frameworks without input of global parameters such as a pipe diameter. The proposed model is implemented in the *MultiMorph* framework based on the OpenFOAM Foundation release open-source CFD library. The performance of the new model is evaluated by conducting own annular flow experiments with void fraction measurements using electrical resistance tomography, as well as with comparison to published models from the literature. Qualitatively, the model can adequately resolve the formation of interfacial waves on the liquid film downstream from the inlet. The simulated droplets are primarily generated at the tip of such waves, which is consistent with the physical understanding and experimental observations of droplet entrainment. Quantitatively, the modeled entrained droplet fraction matches well the experimental observation in the developing entrainment region. The liquid film fraction obtained with the new model is analyzed and compared with the experimental data. Good agreement between measured and simulated statistics of the liquid film fraction, i.e., the mean, standard deviation, probability density function, and power spectral density, is demonstrated.

I. INTRODUCTION

In gas–liquid two-phase flow, there are various flow regimes due to different gas and liquid velocities. Annular flow is an important flow regime that occurs when the gas velocity is relatively high compared to the liquid velocity. It is widely encountered in numerous industrial fields, such as chemical processing, nuclear reactor safety, and natural gas production. Generally, annular flow features a liquid film on the pipe wall and a gas core in the pipe center.[1] The gas core and the liquid film are separated by a gas–liquid interface that is characterized by interfacial waves. If the gas and liquid superficial velocities satisfy certain conditions, droplets can be generated from interfacial waves and can be entrained into the gas core. This process is called droplet entrainment. On the other hand, some droplets in the gas core could return to the liquid film, which is called droplet deposition. Droplet entrainment and deposition play pivotal roles in the mass, momentum, and energy transfer between the gas core and liquid film.

08 April 2024 03:17:13

The modeling of annular flow is still a challenging task because of the complexity of the flow. Based on the characteristics of annular flow, some scholars proposed mechanistic models to predict specific parameters, such as pressure gradient, film thickness, entrainment rate, deposition rate, wave frequency, or velocity. In addition to these mechanistic models, the computational fluid dynamics (CFD) is becoming a powerful approach to model the annular flow predicting its flow properties.

In recent years, extensive CFD analyses of annular flow have been performed by lots of researchers. Due to the complexity, there is no unique numerical method to simulate all physical phenomena of annular flow. Hence, different simulation approaches for various purposes can be found in the literature. Some studies aimed at investigating the interfacial phenomena and reconstructing the interface structure by interface tracking approaches. Volume of fluid (VOF) and level set methods have been used to study the development of interfacial waves,[2–5] entrainment processes,[6–9] deposition processes,[10] and the features of liquid films.[11–14] In some studies interested in the characteristics of the entrained droplets, the Lagrangian framework,[15–17] the lattice Boltzmann method,[18] and the population balance model[19] have been used.

Another category of numerical methods is multifield methods based on the two-fluid model. They allow the coexistence of multiple flow morphologies: gas core, liquid film, and droplets are modeled as separated phases. This approach has great potential to predict the properties of annular flow. Adechy and Issa[20] proposed a three fields model to predict annular flow in vertical and horizontal pipes. In this model, the gas core is represented as a mixture of gas and droplets, where the gas phase is controlled by the Eulerian transport equations, and the droplets are simulated by a Lagrangian method. As for the liquid film, a simplified boundary layer was used. Alipchenkov et al.[21] proposed a model that consists of individual mass, momentum, and energy equations for the gas core, droplets, and liquid film. Their simulation includes a droplet number density to estimate the mean particle size. Höhne et al.[22] used the algebraic interfacial area density (AIAD) framework to simulate annular flow. The gas core, liquid film, and droplets can be accounted for in this framework, and blending functions are defined based on the volume fraction to identify different morphologies. A sub-grid droplet entrainment model was established to simulate the annular flow in horizontal pipes. To predict the dryout in Boiling Water Reactors, Li and Anglart[23] proposed a three-fields model specified for annular flow, where the liquid film is modeled by a two-dimensional film model. The gas core is either simulated with the Eulerian–Eulerian[24] or with the Eulerian–Lagrangian[23] approach. Liquid film evaporation, droplet entrainment, and deposition are considered as source terms in the conservative equations.

Recently, the morphology-adaptive multifield two-fluid model (*MultiMorph*) was established.[25,26] This framework combines the two-fluid model for sub-grid flow structures and VOF-like interface tracking method for large resolvable interfaces. The two-fluid model is combined with the compact momentum interpolation method for multiphase flow,[27] and the strong phase coupling in resolved interfacial regions is realized by a partial elimination algorithm.[28] The *MultiMorph* model allows to simulate an arbitrary number of phases simultaneously, and each phase is represented by its individual set of conservation equations. Due to these advantages, the morphology-adaptive framework is suitable to model the complicated annular flow

and will be applied in this work. For the multifield fields model, closure models that describe interfacial momentum and mass transfer are important to produce reliable results. Recent work improved the morphology adaptive model's performance for interface modeling.[29] However, for modeling annular flows, the morphology-adaptive framework lacks a closure formulation for droplet entrainment. Therefore, an entrainment model should be introduced in this framework.

There are numerous droplet entrainment models available in the literature. However, the majority of existing models are not applicable to resolving CFD simulations, as they are based on integral quantities, such as average film thickness and superficial velocity.[30–34] This features make the aforementioned models suitable for the one-dimensional annular flow simulations, although they are of limited use for three-dimensional modeling approaches that should be based on local hydrodynamic parameters. One classic model that which belongs to this category was proposed by Okawa et al.[30] A rare exception is the sub-grid entrainment model for annular flow proposed by Höhne and Hänsch,[35] which has been implemented and applied in the AIAD model. Their model[35] was developed under the assumption that turbulence is the dominant mechanism to drive droplet entrainment at the free surface, which is an adaption of Ma et al.'s[36] bubble entrainment model. It is assumed that, due to the turbulence, the interface becomes wavy and, hence, forms a bulge. Subsequently, the droplets are generated in a layer close to the interface. In this case, the entrainment rate is related to the turbulence kinetic energy and to the liquid velocity.

At the same time, a generally accepted concept is that the droplet entrainment happens due to the deformation of the gas–liquid interface, which can be understood as a consequence of the interfacial force balance. Five entrainment mechanisms were identified due to the interfacial deformation features:[37] roll wave, wave undercut, bubble burst, liquid impingement, and liquid bulge disintegration. These five mechanisms occur at different flow conditions. Previous studies reported that in a cocurrent annular flow with low viscous fluids or high gas velocities, the droplet entrainment is mainly attributed to the roll wave mechanism.[38,39] On the top of the roll wave, the drag force and surface tension determine the wave deformation. If the gas velocity is high enough and the surface tension is not sufficient to retain the interface structure, the frictional force shears off the crest of the wave, and droplets are formed on the top of the wave. This understanding implies that the droplet entrainment is closely related to interfacial waves and to shear forces. Hence, a sub-grid entrainment model based on the local shear is crucial for a successful multifield modeling of annular flows.

This paper aims to simulate the droplet entrainment in annular flows by means of the *MultiMorph* model. Three phases (continuous gas, continuous liquid, and dispersed liquid) exist simultaneously, and one set of conservation equations is solved for each phase simultaneously. A new sub-grid droplet entrainment model based on the local shear is proposed to predict the entrainment process on the interface. Laboratory experiments are carried out in order to obtain qualitative and quantitative reference data for vertical annular flows. A comparison with experimental data are presented to evaluate the performance of this new entrainment model.

II. NUMERICAL MODEL
A. Morphology-adaptive multifield two-fluid model

In the *MultiMorph* model, annular flows are represented by three phases: liquid film, gas core, and droplets. Here, the liquid film and the

gas core are both modeled as continuous phases, and the droplets are simulated as a dispersed phase. The conservation equations for mass and momentum for each individual phase α are presented in Eqs. (1) and (2), respectively.[25]

$$\frac{\partial r_\alpha \rho_\alpha}{\partial t} + \nabla \cdot (r_\alpha \rho_\alpha \boldsymbol{v}_\alpha) = \Gamma_\alpha, \tag{1}$$

$$\frac{\partial r_\alpha \rho_\alpha \boldsymbol{v}_\alpha}{\partial t} + \nabla \cdot (r_\alpha \rho_\alpha \boldsymbol{v}_\alpha \boldsymbol{v}_\alpha)$$
$$= -r_\alpha \nabla P + \nabla \cdot \boldsymbol{T}_\alpha + r_\alpha \rho_\alpha \boldsymbol{g} + \sum_{\beta \neq \alpha} \boldsymbol{F}_{\alpha\beta} + \boldsymbol{M}_\alpha, \tag{2}$$

$$\Gamma_\alpha = \sum_{\beta \neq \alpha} \Gamma_{\alpha\beta}, \quad \boldsymbol{M}_\alpha = \sum_{\beta \neq \alpha} \Gamma_{\alpha\beta} \boldsymbol{v}_\gamma. \tag{3}$$

Here, r is the phase fraction, ρ is the phase density, v is the phase velocity, Γ is the source term of mass transfer, t is the time, P is the pressure, $\boldsymbol{T}$ is the effective stress tensor, $\boldsymbol{g}$ is the gravitational acceleration, $\boldsymbol{F}$ are the closure forces, and $\boldsymbol{M}_\alpha$ is the momentum source term resulting from the mass source terms. The mass transfer velocity $\boldsymbol{v}_\gamma$ is equal to $\boldsymbol{v}_\beta$ for positive $\Gamma_{\alpha\beta}$ (transfer from phase β to phase α); otherwise, it is equal to $\boldsymbol{v}_\alpha$. Note that the source terms (3) only contribute if a phase transfer is active.

The subscripts α and β represent a specific phase. The present work considers three phases: continuous liquid (l), continuous gas (g), and dispersed droplets (d).

In Eqs. (1) and (2), closure models are used to describe the mass and momentum transfer between phases. The simulation of annular flow should account for the phase interaction between the liquid film and gas (two continuous phases), as well as the interaction between droplets and gas (dispersed phase in a continuous phase).

B. Closure models for liquid film and gas
1. Surface tension

The surface tension model from Brackbill et al.[40] is adopted,

$$\boldsymbol{F}_{\alpha\beta}^\sigma = r_\alpha \sigma_{\alpha\beta} \kappa_{\alpha\beta} \hat{\boldsymbol{n}}_{\alpha\beta}. \tag{4}$$

The sub-script $\alpha\beta$ indicates that the transfer is considered between the phases α and β. $\kappa_{\alpha\beta}$ is the interface curvature. It is computed from

$$\kappa_{\alpha\beta} = \nabla \cdot \hat{\boldsymbol{n}}_{\alpha\beta}. \tag{5}$$

Here, the $\hat{\boldsymbol{n}}_{\alpha\beta}$ is the unit vector normal to the interface, which is calculated from the phase fraction gradient, $\frac{\nabla r}{|\nabla r|}$. For the considered air-water system, a constant surface tension coefficient $\sigma_{\alpha\beta} = 0.072\,\text{N/m}$ is used.

2. Drag force between gas core and liquid film

The drag closure model of Ishii and Mishima[41] is used to describe the drag force between the gas core and the liquid film

$$\boldsymbol{F}_{\alpha\beta}^{D,IM} = -C_D^{IM} \frac{\rho_{\alpha\beta}}{2} a_I ||\boldsymbol{v}_{\alpha\beta,\text{slip}}|| \boldsymbol{v}_{\alpha\beta,\text{slip}}. \tag{6}$$

The drag coefficient is denoted by C_D^{IM}, $\rho_{\alpha\beta}$ is referred to as the volume-fraction weighted density between phases α and β, $\boldsymbol{v}_{\alpha\beta,\text{slip}}$ is the slip velocity between the gas phase and the liquid film, and a_I denotes the interfacial area density.

In annular flows, the interface is relatively wavy and rather deformed, so the drag coefficient would be larger than the coefficient of a regular shaped sphere. Based on this approximation, Ishii and Mishima[37] suggested that the drag coefficient equals to one. Hence, in the current simulation, $C_D^{IM} = 1$ is adopted for the wavy interface in annular flow.

3. Turbulence modeling

The $k - \omega$ SST (Shear Stress Transport) RANS model of Menter[42] is used to simulate the two-phase flow turbulence. To improve the turbulence modeling near the interface, turbulence damping should be taken into consideration. For this purpose, an additional damping term can be added to the turbulence equations to model the wall-like damping effect near the interface. The damping term formulation of Frederix et al.[43] is applied to the ω equation in the $k - \omega$ SST turbulence model by Tekavčič et al.,[29] as shown in Eqs. (7) and (8). This formulation is used hereafter.

$$\frac{\partial r_\alpha \rho_\alpha \omega_\alpha}{\partial t} + \nabla \cdot (r_\alpha \rho_\alpha \boldsymbol{v}_\alpha \omega_\alpha)$$
$$= \nabla (r_\alpha (\mu_\alpha + \sigma_\omega \mu_\alpha^T) \nabla \omega_\alpha) + \frac{r_\alpha \rho_\alpha \gamma}{\mu_\alpha^T} \tilde{P}_\alpha - \beta r_\alpha \rho_\alpha \omega_\alpha^2$$
$$+ 2(1 - F_1) \frac{r_\alpha \rho_\alpha \sigma_{\omega 2}}{\omega_\alpha} \nabla k_\alpha \cdot \nabla \omega_\alpha + S_\alpha^\omega, \tag{7}$$

$$S_\alpha^\omega = A r_\alpha \beta \rho_\alpha \left(\frac{\nu_\alpha}{\beta \delta_\alpha^2}\right)^2. \tag{8}$$

Here, μ_α denotes the dynamic molecular viscosity of phase α, μ_α^T is the eddy viscosity, and k_α is the turbulent kinetic energy. The model coefficients are β, $\sigma_{\omega 2}$, σ_ω, γ, and F_1, and $\tilde{P}_\alpha$ is the turbulent kinetic energy production term of the $k - \omega$ SST model. The interface indicator field is referred to as A, $\nu_\alpha = \mu_\alpha / \rho_\alpha$ is the kinematic viscosity, and δ_α is the damping length scale. In the simulation, the damping term is set to $10^{-4}\,\text{m}$ and applied in the gas phase only.

C. Momentum closure models for droplets in gas

The closure models for droplets and gas are selected according to Agostinelli.[44] The drag force for droplets and gas is calculated by

$$\boldsymbol{F}_{\alpha\beta}^{D,SN} = \frac{3}{4} \frac{C_D^{SN}}{d} r_\alpha \rho_\beta ||\boldsymbol{v}_{\alpha\beta,\text{slip}}|| \boldsymbol{v}_{\alpha\beta,\text{slip}}, \tag{9}$$

where α is the droplet phase with droplets of diameter d, and β is the gas phase. Here, $\boldsymbol{v}_{\alpha\beta,\text{slip}}$ is the slip velocity between the gas phase and droplets. The drag coefficient C_D^{SN} is selected according to Schiller and Naumann[45]

$$C_D^{SN} = \begin{cases} \dfrac{24}{Re_d} \left(1 + 0.15 Re_d^{0.687}\right), & \text{if } Re_d \leq 1000 \\ 0.44, & \text{else,} \end{cases} \tag{10}$$

with the Reynolds number Re_d computed based on the droplet diameter.

III. DEVELOPMENT OF THE ENTRAINMENT MODEL

For the simulation of annular flow, closure models for the mass transfer between the droplets and liquid film should be added.

There are two important mass transfer mechanisms in annular flow: droplet entrainment and droplet deposition. It should be noted that it is difficult to discriminate and investigate the two contradictory phenomena in one case, since droplet entrainment and deposition happens simultaneously. This work focuses on the droplet entrainment; the droplet deposition is ignored so that the entrainment model can be studied independently. In this section, a new droplet entrainment model designed for the sub-grid CFD simulation is established based on the shear-off mechanism.

A. Droplet entrainment model for under-resolved interfaces

The goal of the present work is to find an empirical droplet entrainment model, which

(1) captures the main entrainment mechanisms,
(2) only bases on locally available quantities, and
(3) is applicable even on coarse meshes.

It has been proven that the Weber number is the decisive parameter to predict droplet entrainment rates.[30–32] The number's definition is problem-dependent, but can be understood as the ratio of destabilizing kinetic energy to stabilizing surface energy. Entrainment models of the aforementioned type are based on the assumption that the generated droplet mass per unit time and unit interfacial area, $\dot{m}_d$, is proportional to an interfacial Weber number, We_I

$$\dot{m}_d = C_E \rho_l U We_I. \tag{11}$$

The constant dimensionless parameter C_E is expected to be case-dependent and is determined later in Sec. V A. The characteristic velocity U is defined as the ratio of the kinematic liquid viscosity ν_l to the capillary length scale L_a, as shown in Eq. (12), which is motivated by the scaling suggested by Okawa et al.,[30]

$$U = \frac{\nu_l}{L_a} \quad \text{with} \quad L_a = \sqrt{\frac{\sigma}{||\boldsymbol{g}||(\rho_l - \rho_g)}}. \tag{12}$$

The Weber number is usually computed from the superficial gas velocity resulting in a global (integral) Weber number definition. However, for the present work, a local criterion is required. Therefore, the interfacial Weber number is defined according to

$$We_I = \frac{\rho_g ||\boldsymbol{v}_l^+ - \boldsymbol{v}_g^+||^2 L_a}{\sigma}. \tag{13}$$

Here, $\boldsymbol{v}_l^+$ and $\boldsymbol{v}_g^+$ denote the velocity vectors on the liquid and gas sides of the interface, respectively. These values are communicated across the width of the interface, as suggested by Meller et al.[46] The difference $||\boldsymbol{v}_l^+ - \boldsymbol{v}_g^+||$ can be seen as a measure for the under-resolved relative interface velocity. It has a finite value in the case of coarse mesh resolutions and vanishes on very fine meshes. Again, the length scale in Eq. (13) is set to the capillary length L_a defined in Eq. (12).

The entrainment rate in Eq. (11) is an area-specific mass source (kg s^{-1} m^{-2}). The corresponding volume-specific mass source Γ_d (kg s^{-1} m^{-3}) is obtained by multiplication with the interfacial area density. For a continuous interface, the interfacial area density is equal to the magnitude of the volume fraction gradient $||\nabla r_l||$. This allows to write

$$\Gamma_d = ||\nabla r_l|| \dot{m}_d = ||\nabla r_l|| \frac{\rho_l \nu_l}{L_a} C_E We_I, \tag{14}$$

which is the volume-specific formulation of the interfacial droplet generation. The liquid is reduced accordingly

$$\Gamma_l = -\Gamma_d. \tag{15}$$

This transfer from continuous liquid to disperse liquid is applied in cells where the following conditions are fulfilled,

$$r_l > \varepsilon \quad \text{and} \quad \langle r_g \rangle = \frac{\sum_f A_f \lfloor r_g \rfloor_f}{\sum_f A_f} > 0.01. \tag{16}$$

The first condition ensures that there is at least some continuous phase (water) in the cell, which can be converted to the disperse state (droplets). The residual value ε is set to 10^{-6}. The second equation describes a face average of the continuous gas fraction computed from the cell face area A_f and the volume fraction values interpolated to the face $\lfloor r_g \rfloor_f$. It ensures that the cell is located in the vicinity of a continuous interface (air in the present case). Note that the interpolation step $\lfloor r_g \rfloor_f$ is crucial to make sure that neighbor cells are also considered.

Experiments from previous works[32] suggest that the droplet rate does not increase anymore if the Weber number reaches a critical value, i.e., the entrainment rate saturates at a given Weber number. Wang et al.[32] reported an upper limit of approximately $\rho_l \nu_f / (2L_a)$. However, such a limit is not considered in the present work as it was not observed in the experiments described below.

B. Robust implementation of interfacial mass transfer

A procedure for a reliable interfacial mass transfer implementation is proposed. It avoids the problems occurring with the naive implementation.

1. The problem of empty interfacial cells

A given interfacial mass transfer $\dot{m}_d$ can be translated to a volume source Γ_d according to

$$\Gamma_d = ||\nabla r_l|| \dot{m}_d. \tag{17}$$

This ensures that the generated mass scales with the area of the interface (and not with the cell volume). However, the implementation of Eq. (17) is not sufficent. Practical tests reveal that the mass rate observed in the simulation is under-estimated and oscillates. The oscillations are stronger on coarse meshes. This is visible in the demonstration test case discussed below (Fig. 2, top). The reason is the following: to realize a specific mass of droplets according to a given rate, each cell with non-zero $||\nabla r_l||$ needs to contribute to the phase transfer. However, if an interface cell with $||\nabla r_l|| \neq 0$ does not contain any continuous water ($r_l = 0$), then there is no material to create droplets from. This situation is sketched in Fig. 1: the interfacial area density $||\nabla r_l||$ computed for the cell C from the interpolated r_l values is non-zero, but there is no continuous material, which can be transferred to disperse material.

2. Improvement

The idea is to identify interfacial cells without continuous water, and let the next non-empty neighbor cell realize the missing
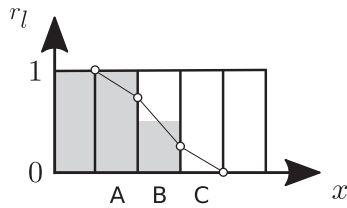
FIG. 1. Volume fraction distribution (gray) and face-interpolated values (circles) for a given diffuse interface. Cells *A, B,* and *C* are interface cells (non-zero values for the interfacial area density $||\nabla r_l||$ computed from interpolated volume fraction). No disperse material can be created in cell *C* because there is no continuous material that can be transferred to droplets.

proportion of the transfer in addition. In Fig. 1, for example, there are three interface cells (*A, B, C*), each with a specific value of $||\nabla r_l||$ computed from the interpolated continuous void fraction. Cell *C* cannot contribute to the transfer as there is no continuous material available. Instead, the missing amount of disperse material (supposed to be created in cell *C*) has to be additionally created in cell *B*. This is done by adding the interfacial area density of cell *C* to the interfacial area density of cell *B*: $||\nabla r_l||'_B = ||\nabla r_l||_B + ||\nabla r_l||_C$.

In the three-dimensional finite-volume context, this reads

$$||\nabla r_l||' = ||\nabla r_l|| + C, \qquad (18)$$

with a correction term C. The first step is to find empty neighbors. A cell is considered as empty, if the extrapolated value

$$r_l^{\text{extrapolated}} \approx \lfloor r_l \rfloor_f - \frac{\Delta_f}{2} ||\nabla_{\mathbf{n}} r_l||_f, \qquad (19)$$

is below the residual ε (set to the same very small value as before). Note that the magnitude of the gradient is used in Eq. (19) to obtain an efficiently implementable expression that is symmetric with respect to adjacent cells. It can be shown that this has no effect on the final correction term. The interfacial area density of an empty cell can be approximated by

$$||\nabla r_l||_{\text{empty neighbour}} \approx \frac{r_l}{2\Delta_f}, \qquad (20)$$

with the neighbor cell distance Δ_f. This expression is obtained from the difference of the face-interpolated volume fractions (assuming an equidistant mesh and that an empty interface cell is surrounded by $r_l \neq 0$ on the one side and $r_l = 0$ on the other side similar to cell *C* in Fig. 3). These contributions need to be summed up for all empty neighbor cells

$$C = \frac{r_l}{2} \sum_f \frac{1}{\Delta_f} \text{pos}\left(\varepsilon - r_l^{\text{extrapolated}}\right). \qquad (21)$$

Note that $\text{pos}(x)$ gives 1 if $x > 0$ and zero otherwise. Hence, $\text{pos}(\varepsilon - r_l^{\text{extrapolated}})$ gives 1 if the cell face is adjacent to an empty cell. This procedure allows to represent the total amount of interfacial area density on cells with non-zero continuous material. Overall, there are three steps: extrapolation of the liquid fraction [Eq. (19)], collection of the interfacial area density contribution of each empty neighbor cell [Eq. (21)], and correction of the local interfacial area density (18). An efficient way to compute [Eq. (21)] is to compute the expression $\text{pos}(\varepsilon - r_l^{\text{extrapolated}})/\Delta_f$ for each cell face first, before evaluating C for each cell.
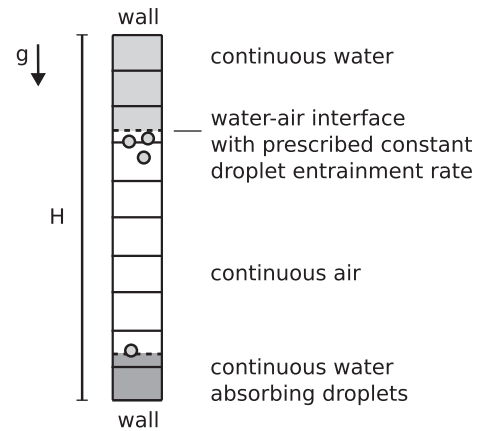

FIG. 2. Basic test with a prescribed constant droplet entrainment rate.

3. Demonstration

It is demonstrated by means of a one-dimensional test case with a prescribed constant droplet entrainment rate (Fig. 2, $H = 1$ m). Droplets are created at a hanging free interface, before falling down into a continuous reservoir. The upper continuous water layer cannot move downward as it is strongly coupled to the continuous water. The same mesh study is carried out for the case without correction and with the described correction (Fig. 3). The number of cells in the vertical direction is doubled three times. Without the proposed correction, the entrainment rate is underestimated, oscillates, and has problems when the upper water reservoir runs dry (Fig. 3, top, slope changes at approximately 2 s). The proposed correction of the interfacial area density significantly improves the situation and allows to realize the prescribed constant entrainment rate (Fig. 3, bottom).
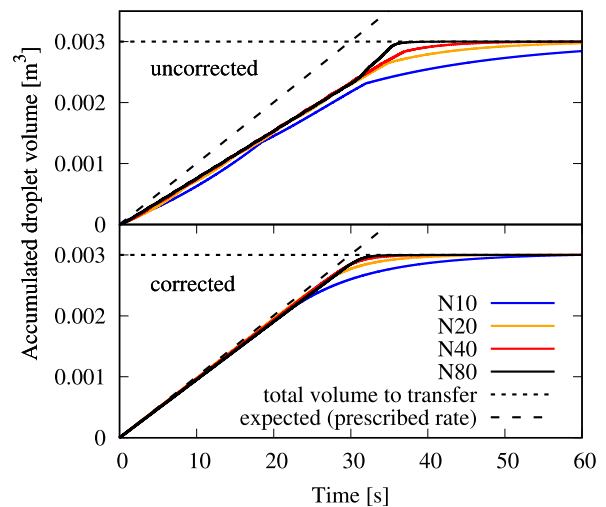

FIG. 3. Accumulated droplet volume over time without the proposed correction (top) and with the proposed interfacial area density correction (bottom).
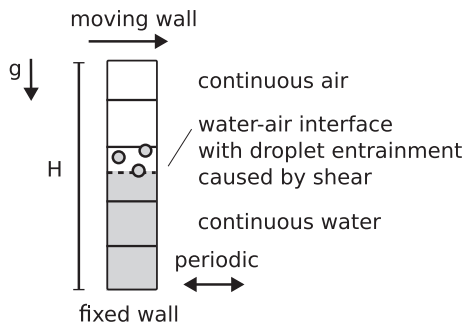
FIG. 4. Basic test with shear-induced droplet entrainment.

C. Properties of the proposed model

The basic properties of the model proposed in Eq. (14) are assessed in the following. The difference to a constant rate model is the dependence of the rate on the interfacial Weber number. A generic test case is considered to demonstrate the consequences. This two-dimensional demonstration case features a water–air stratification, where the upper air layer is driven by the moving top wall. The bottom wall is at rest, and periodic boundary conditions are applied in the horizontal direction. The proposed model is active on the continuous interface, which is initially placed in the center of the domain. The domain has a height of $H = 22$ mm. The situation is sketched in Fig. 4.

The moving top wall results in a shear flow producing non-zero values for the interfacial Weber number We_I. A refinement study with $N = 5, 11, 23,$ and 47 cells in the vertical direction is performed so that the interface is always located in the center of the center cell to allow comparison. Here, the interfacial Weber number We_I is recorded (Fig. 5). The better the shear flow is resolved, the lower the value. The entrainment rate scales accordingly (not shown). The mesh dependency of the interfacial Weber number is in principal desired as it is designed with the hope to detect under-resolved situations. Future work will show whether this approach can help to realize a continuous transition into fully resolved entrainment regimes. However, this is strongly connected to resolution-adaptive momentum coupling,[46] which is not part of the present work. Note that implementation and testing were carried out carefully (see Sec. III) to make sure that the interfacial Weber number is the only highly mesh-dependent quantity. The proposed model is applied in a more complex setup in the following.
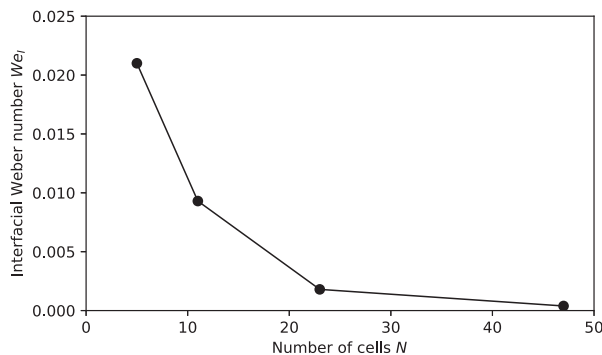
IV. LABORATORY EXPERIMENTS AND NUMERICAL SETTINGS

Laboratory experiments were conducted to evaluate the performance and characteristics of the proposed entrainment model. The experimental setup and conditions, and the corresponding numerical case are presented in the following.

A. Experimental facility and geometry settings

Figure 6 shows the flow loop of the experiment, which consists of supply systems, test section pipes, and measuring devices. Tap water and air are used as the liquid and gas phases, respectively. A centrifugal pump is used to supply water from a water tank, and a screw air pump is adopted to introduce high speed air to the flow pipe. Atmospheric pressure and ambient temperature are used as the operational pressure and temperature, respectively. The test section pipe is made of transparent plexiglass, so that the flow structure can be captured by visual observation. As shown in Fig. 6, the test section consists of a circular pipe with an inner diameter $D = 50$ mm and a wall thickness of 10 mm. It is vertically oriented with the length of 3.5 m. The pipe length is $70 D$, suitable for fully developing an annular flow. A mixture of gas and liquid is injected at the inlet section at the bottom of the vertical pipe to form the co-current annular flow. Eventually, the air is released into the atmosphere, and the water flows back to the tank.

An electrical resistance tomography (ERT) instrument is located at $z = 3$ m, with z being the streamwise direction, to obtain the integral void fraction. Its inner diameter is the same as that of the flow pipe, i.e., 50 mm. Compared with other multiphase measuring, such as wire mesh and conductivity probes, a primary advantage of ERT is that it uses non-intrusive technology so that the phase distribution can be measured without disturbing the interior flow.[47,48] The original signal acquired from the electrodes by a data acquisition system is processed by a post-processing software. A digital single-lens reflex camera is
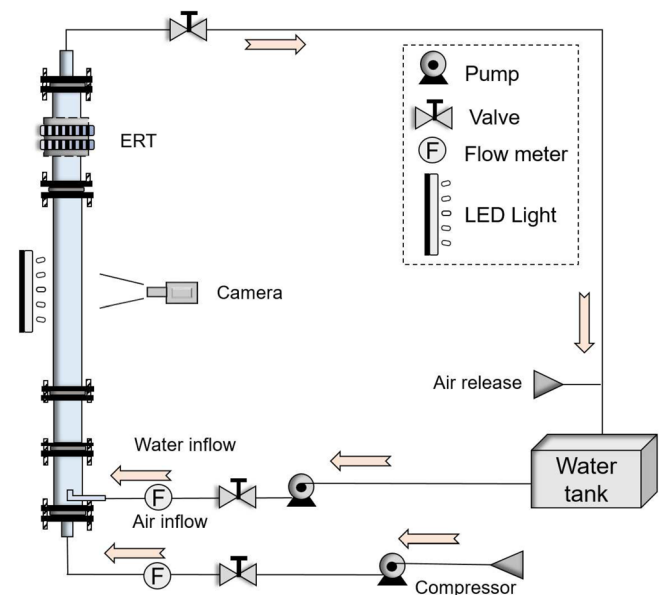

FIG. 5. Interfacial Weber number for different mesh resolutions.

FIG. 6. Schematic of the experimental flow loop.

located in front of the transparent pipe. A shadowless lamp is placed behind the transparent pipe to provide sufficient light, so different interfacial structures could be discriminated by visualization. To observe the interfacial structures clearly, the photo mode of the camera is set at a shutter speed of 1/6000 s to obtain high-resolution photos. More details about the experimental setup and measurements using ERT can be found in previous studies.[49]

Figure 7 shows the geometry of the computational domain, corresponding to the flow pipe in Fig. 6. At the bottom, an inlet pipe with a length of 0.15 m is attached. Water is injected via a water annulus, and air enters the domain through the inner pipe section. In the inlet section, water and air channels are separated via a thin baffle that acts as an internal no-slip boundary. In accordance with the experiment, the flow pipe is 3.5 m long. In order to observe the spatial development of the pipe flow, sample data are extracted along radial lines at the following locations downstream the inlet section of the pipe: z = 0.01, 0.5, 1.0, 1.5, 2.0, 2.5, 3.0, and 3.49 m. For the simulation, the operating point with respective superficial velocities of $v_{sg} = 22.64$ and $v_{sl} = 0.17$ m/s for gas and liquid is selected.

B. Initial and boundary conditions

The inlet velocities of gas and liquid are calculated by the superficial phase velocity and the area occupied by each phase, as shown in the following equations:

FIG. 7. Simulation geometry, where the red region indicates gas inflow, and the yellow region is water inflow. Three sampling locations are shown exemplary.

$$v_{g,in} = \frac{v_{sg}D^2}{(D - 2\delta)^2},\qquad(22)$$

$$v_{l,in} = \frac{v_{sl}D^2}{D^2 - (D - 2\delta)^2}.\qquad(23)$$

The superficial velocities of gas and liquid are denoted v_{sg} and v_{sl}, respectively, and D is the pipe diameter. The thickness of the water inlet is referred to as δ.

The outlet condition is specified to ensure a constant mean value of pressure. Neumann type boundary conditions are used for the remaining fields. Table I presents the initial-phase specific turbulent kinetic energy k_α and specific dissipation rate ω_α. The phase-specific turbulent kinetic energy k_α is predicted from the turbulence intensity I_α, as shown in Eq. (24).[29] The specific dissipation rate was calculated by Eq. (25),[29] assuming a fixed value for μ_α^T/μ_α. The pipe wall is set as no-slip condition, and the wedge faces are set as axis-symmetry boundaries.

$$k_\alpha^{in} = \frac{3}{2}\left(v_\alpha^{in}I_\alpha\right)^2,\qquad(24)$$

$$\omega_\alpha = \frac{\rho_k k_\alpha}{\mu_\alpha}\left(\frac{\mu_\alpha^T}{\mu_\alpha}\right)^{-1}.\qquad(25)$$

C. Grid generation

The uniform mesh size in the axial direction is 2 mm. To achieve a higher mesh resolution toward the wall and to represent the gas–liquid interface more accurately, more grid cells are required close to the pipe wall. Hence, the expansion ratio is applied in the radial direction. In this case, expansion ratios of 0.2 and 0.5 are used for the inner and outer tube, respectively. As a result, the inner and the outer tubes are resolved with 12 and 4 cells, respectively. This results in a total number of 26 957 grid cells. The robustness of the results was proven in a preliminary refinement study with two refinement levels confirming the properties reported in Secs. III B and III C.

V. RESULTS AND DISCUSSION

The new entrainment model is evaluated in this section by comparing it with experimental data and correlations from published studies. For this purpose, the results and discussions are arranged in five parts: in Sec. V A, a parameter study is carried out to determine model coefficients. Subsequently, the performance of the new model is
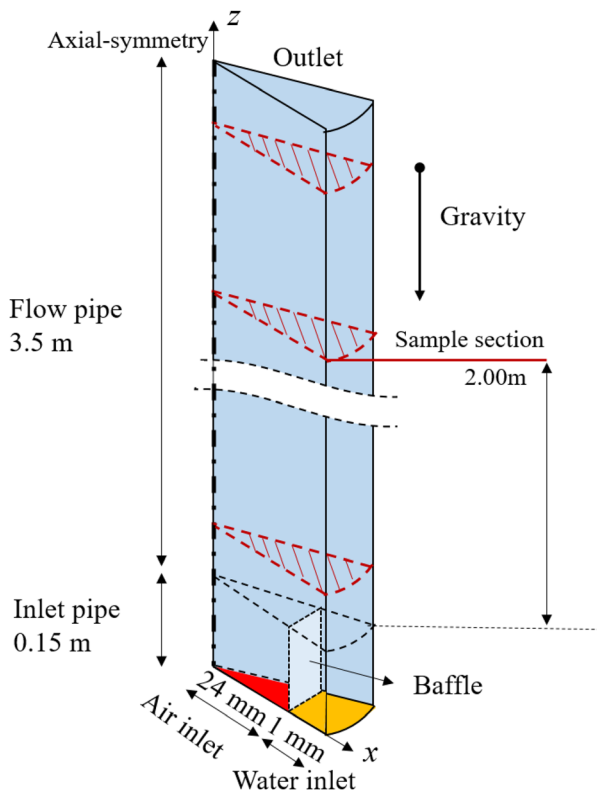
TABLE I. Material properties and inlet conditions.

Quantity	(unit)	Air (g)	Water (l, d)
ρ_α	(kg m^{-3})	1.204	998.3
v_{in}	(m s^{-1})	24.5659	2.1683
I_α	(-)	0.05	0.05
$\frac{\mu_\alpha^T}{\mu_\alpha}$	(-)	10	10
μ_α	(Pa s)	1.824×10^{-5}	1.002×10^{-3}
k_α	(m^2 s^{-2})	2.2631	0.0176
ω_α	(s^{-1})	1.4938×10^4	1.7566×10^3

discussed in Secs. V B and V C, where qualitative and quantitative results are shown, respectively, and compared with the experimental data.

A. Parameter study

As mentioned in Sec. III, the entrainment coefficient, C_E, should be determined before using the new entrainment model. In this section, the influence of C_E is investigated. The entrainment fraction, which directly influences the amount of droplets, is used as a measure to study the model coefficients. For this purpose, the entrainment fraction is experimentally investigated before a comparison is drawn to the simulation results.

1. Entrainment fraction from the experiment

The entrainment fraction is defined as the ratio of droplet mass flow rate to the total liquid mass flow rate. This parameter quantifies the amount of dispersed droplets, which are transferred from the continuous film to the dispersed phase. As the droplet entrainment fraction cannot be measured directly in the experiment, this quantity is estimated via correlations from the literature.

Some works have shown that the entrainment behavior is influenced by the entrance effects close to the inlet section,[38,50] so that there are two regions for entrainment fraction. The first region is called developing entrainment region, which is close to the flow entrance. In this area, the annular flow is not fully developed, and the entrainment fraction is not a constant value. Furthermore, in a certain distance downstream from the inlet, the so-called fully developed entrainment region is found. Here, the entrainment fraction remains constant because entrainment and deposition mechanisms reach an equilibrium state. A large number of correlations can be found in the literature to estimate the entrainment fraction in the developing entrainment region and the fully developed entrainment region. For the developing entrainment region, Kataoka et al.[34] related the entrainment fraction to the axial distance, z, from the inlet, by

$$E_z = \left[1 - \exp(-1.87 \times 10^{-5}\xi^2)\right] E, \tag{26}$$

where E is the entrainment fraction in the fully developed region, and ξ is the dimensionless distance calculated according as

$$\xi = \frac{z\,Re_l^{0.5}}{D\,We_g^{0.25}}. \tag{27}$$

Here, We_g is the Weber number of the gas phase, and Re_l is the Reynolds number of the liquid phase.

The transition from the developing entrainment region to the fully developed entrainment region is located at a so-called critical distance z_{cri}. According to Kataoka et al.'s work,[34] this quantity is calculated with the following equation:

$$z_{cri} = \frac{440\,D\,We_g^{0.25}}{Re_l^{0.5}}. \tag{28}$$

For the fully developed region, Aliyu et al.[51] established a correlation to estimate the entrainment fraction in various flow conditions and pipe sizes,

$$E = \frac{\chi}{1+\chi}, \tag{29}$$

with

$$\chi = \begin{cases} 0.01\,We^{0.33}\,Re_l^{0.27} & \text{if } u_{sg} > 40\,\mathrm{ms^{-1}} \\ 1.25 \times 10^{-3}\,We^{0.15}\,Re_g^{0.20}\,Re_l^{0.23} & \text{otherwise.} \end{cases} \tag{30}$$

With Eqs. (26)–(30), the entrainment fraction, E_z, along the pipe axial direction, z, can be estimated. As shown in Fig. 8, the critical distance of the transition is 1.92 m, as plotted by the dotted black line. Below the critical distance line, there is the developing entrainment region. The entrainment fraction increases monotonically with increasing axial distance, z. When the z-axis coordinate is close to the critical line, the growth gradient of the entrainment fraction decreases. In the fully developed entrainment region, the entrainment fraction is independent of the axial distance, z. These characteristics will be used to compare the experimental data with the simulation results.

2. Entrainment fraction from the simulation

To study the entrainment coefficient, C_E, three simulations with values of $C_E = 0.01$, 0.1, and 0.18 are carried out. Due to the entrainment model, droplets are generated in the pipe flow. As shown in Fig. 7, several sample sections are defined along the pipe axial direction, z. At each sample section, the entrainment fraction is calculated as

$$E = \frac{W_d}{W_l} = \frac{W_d}{W_f + W_d}. \tag{31}$$

The mass flow rate of droplets and liquid film are denoted W_d and W_f, respectively. Both quantities are calculated according to the following equation:
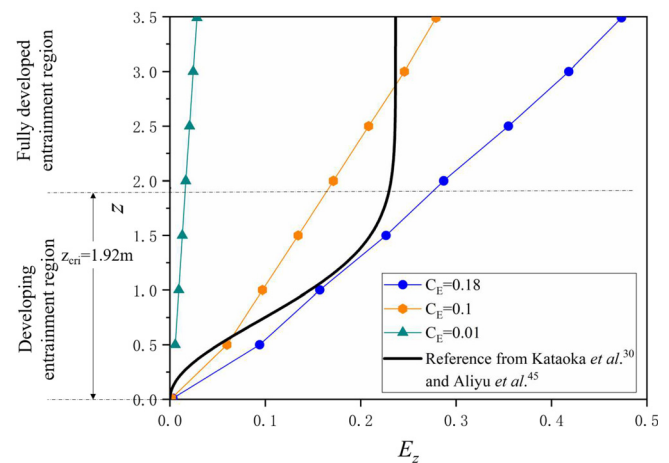
$$W_\alpha = \sum r_\alpha v_\alpha A_c. \tag{32}$$

FIG. 8. The entrainment fraction from the experiment and simulation with different C_E.

In Fig. 8, the entrainment fraction is plotted along the axial coordinate, z, for different entrainment coefficients, C_E, together with the experimental results.

It is evident that the entrainment fraction, E_z, decreases with the reducing entrainment coefficient C_E. When the entrainment coefficient is decreased from 0.18 to 0.01, the magnitude of entrainment fraction decreases from 0.1 to 0.01. For $C_E = 0.01$, the entrainment fraction is relatively small, meaning that less liquid phase is transferred from the liquid film to the droplet phase. For $C_E = 0.18$, the magnitude of the entrainment fraction is close to the experimental results below the critical length, z_{cri}.

However, when reaching the fully developed entrainment region, the CFD results keep the increasing tendency, and it could be inferred that the entrainment fraction would increase to unity if the pipe is long enough. This is different from the experimental results in Sec. V A 1, where the entrainment fraction should be constant across the fully developed region. This phenomenon could be explained by the droplet deposition being ignored in current work, so that the generated droplets cannot be transferred back to liquid film. It is reasonable to introduce a deposition model to simulate annular flow. However, the goal of the present work is to evaluate the newly proposed entrainment model. An additional deposition model will increase complexity considering it is difficult to discriminate the simultaneous effects of entrainment and deposition. Therefore, the deposition process might be focus of future investigations. Overall, Fig. 8 shows that simulated entrainment fraction with $C_E = 0.18$ is well predicted in the developing entrainment region when compared to the experimental results from Sec. V A 1, although the deposition is ignored. Hence, the entrainment coefficient is fixed to $C_E = 0.18$.

Figure 9 shows the comparison between different entrainment models that all exhibit monotonous growth of entrainment fraction with axial distance. The entrainment fraction obtained with the model of Okawa et al.[30] is relatively small, while the values obtained with Höhne and Hänsch's model[35] are larger than the reference data for $z > 0.75$ m. In the developing entrainment region, i.e., $z < 1.92$ m, the new model performs well in accordance with the experimental data compared to the correlations from the literature.
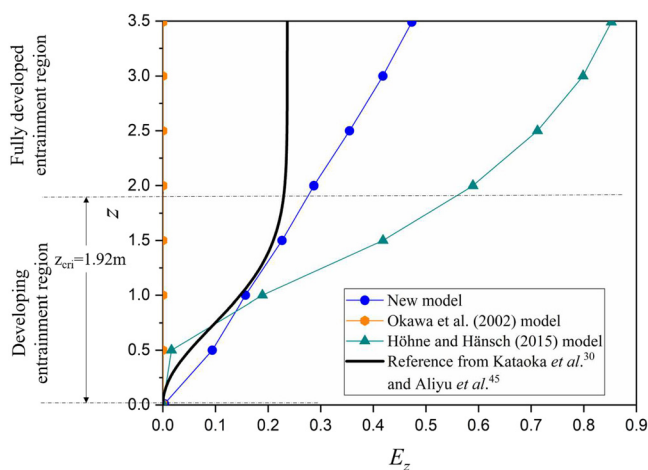
B. Qualitative results

1. Visualization of interfacial wave

In this section, the new model's performance is assessed by comparing it with the experimental results. The entrainment process is closely related to the interfacial waves as reported in the literature. Hence, the qualitative analysis focuses on the interfacial waves.

In Fig. 10, the interfacial waves obtained with the *MultiMorph* model are compared to the experimental results. It can be seen in Fig. 10(a) that the liquid film is relatively wrinkled due to the occurrence of interfacial waves. Previous studies have shown that the interfacial waves can be divided into two categories:[52] the first category is called ripple, which is characterized by high frequency and small amplitude; the second one is called disturbance wave, which is characterized by waves of larger size and higher amplitude. Figure 10(a) shows a typical disturbance wave in the experiment, which can be discriminated by the dark-grey region. It can be seen that the axial size of the disturbance wave is around 30 mm. It should be noted that Fig. 10(a) shows only an outside view of the pipe, while the inner structure of the interface is not directly visible. The numerical simulation helps to gain more insight into the inner structure of the annular flow.

Using the *MultiMorph* model, the interfacial waves are directly resolved on the computational grid. The benefit of the numerical approach is that the dispersed droplets can be modeled as a separate numerical phase. In Fig. 10(b), the simulation result in terms of liquid film fraction is shown for the scenario of a typical disturbance wave. It can be seen that the axial dimension of the modeled wave is around 40 mm, which is similar to the experimental observation. It is clear that the shape of the interfacial wave agrees with the streamlines of the velocity of the gas core. Specifically, the wave exhibits the rolling tendency in the upward direction with a sharp tip, which is caused by the high shear effect from the gas core. Figure 10(c) shows the droplet fraction around the disturbance wave. The majority of the droplets is observed at the tip of the large wave, where they are mainly generated. The droplets, just like the disturbance waves, tend to move upward. Overall, the results presented in Fig. 10 demonstrate that wave structures and droplet generation are captured sufficiently well with the new entrainment model.

2. Development of the interfacial waves

In this section, the evolution of interfacial waves and droplets is analyzed. Figure 11 shows the axial development of the interfacial wave along the pipe. In the range of $0D$–$3D$, the liquid film is shown near the pipe inlet. Here, the film is relatively smooth without large waves. Further downstream, in the range of $10D$–$13D$, there are several waves with small amplitude. From that follows that the interfacial wave is developing between $10D$ and $13D$. Between $z = 40D$ and $43D$, disturbance waves with large size and amplitude are observed. This is in line with observations reported in the literature by Alekseenko et al.[53]

Figure 12 shows the evolution of a single disturbance wave over time, which exhibits the deformation process of the large wave. In Fig. 12(a), the interfacial wave has a smooth shape. Subsequently, with progressing time, the wave travels downstream and becomes gradually deformed. As presented in Figs. 12(b)–12(d), the wave tip stretches in the downstream direction, while moving in the same direction. Especially in Figs. 12(e) and 12(f), the wave is highly deformed with the tendency to shear off.
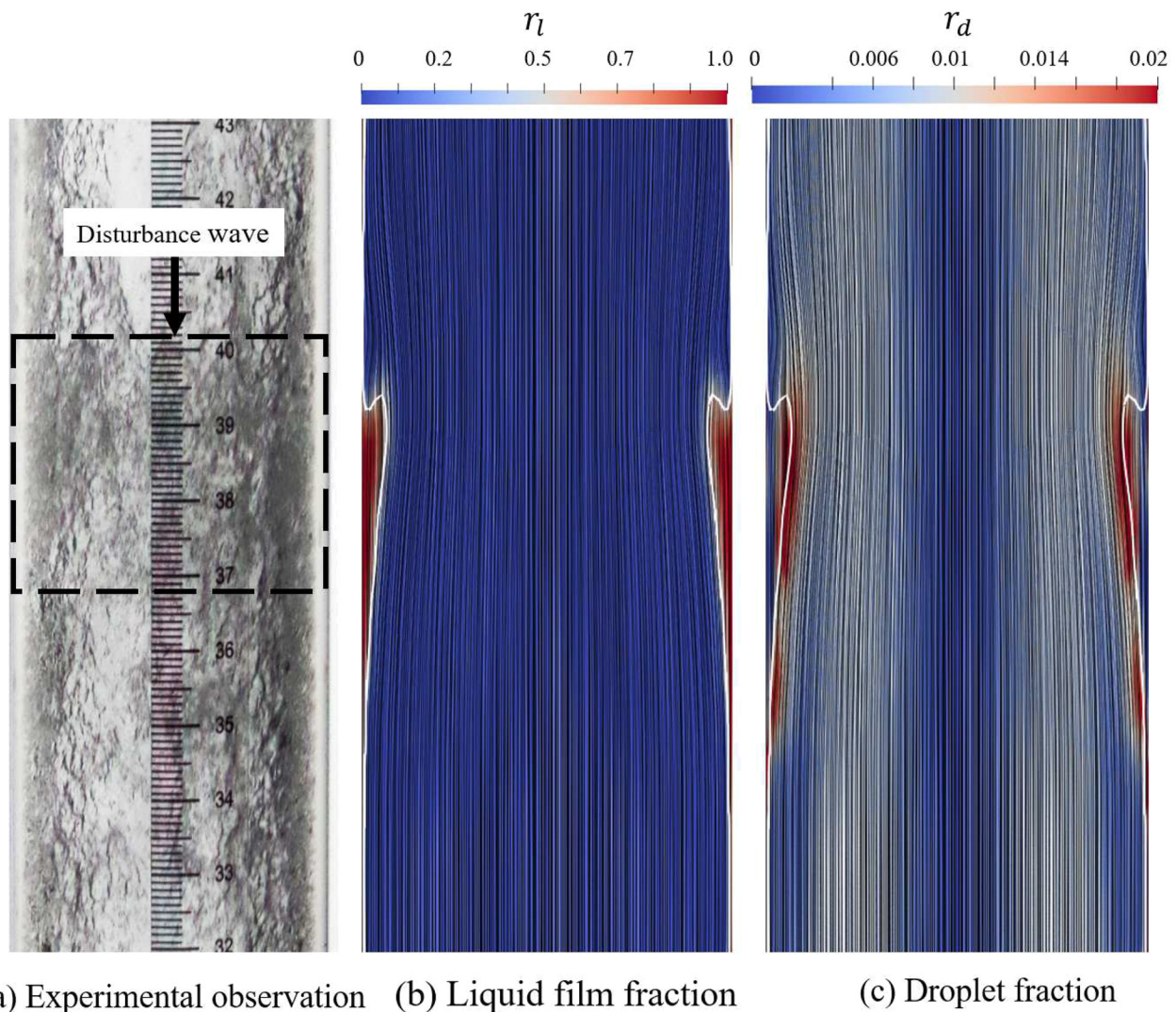

FIG. 9. Entrainment fraction from different models.

(a) Experimental observation   (b) Liquid film fraction   (c) Droplet fraction

FIG. 10. Comparison of interfacial wave between experiment and CFD simulation. Here, (a) shows the snapshot from the camera, while (b) and (c) show the simulated liquid film fraction and droplet fraction, respectively, together with the velocity streamlines in the gas core. The white line marks the iso-line, where the liquid film phase fraction equals 0.5, representing the gas–liquid interface.

3. Generation of the droplets

The droplet fractions during the wave development process are plotted in Fig. 13. Initially, the droplets distribute almost uniformly on the top of the wave, as shown in Fig. 13(a). With progressing time, with the disturbance wave getting highly deformed, the droplet fraction on the tip of the wave front increases significantly, which can be observed in Figs. 13(b)–13(d). With subsequent upward movement of the wave, as presented in Figs. 13(e) and 13(f), the generated droplets are entrained by the gas flow and move to the pipe center. In order to assess the location of entrainment, Fig. 14 presents the distribution of the entrainment rate. During the wave development process, the largest entrainment is always observed on the top of the wave. When the wave is highly deformed by the shear force of the gas flow, the location of highest entrainment rate shifts to the wave front.

Overall, Figs. 13 and 14 show that the generation of droplets is closely related to the disturbance wave, and the maximum entrainment rate is at the crest of the wave. The highest rate of droplet entrainment into the gas flow is observed, when the wave is highly deformed. That is plausible as in shear flow, a wave undergoes a strong deformation before droplets will be sheared off.

4. Comparison of interface behavior among different models

Figure 15 shows snapshots of distributions of droplet phase fraction and entrainment rate from the three models. The main difference is observed in the distribution of the entrainment rate and, hence, of the droplets themselves. With the new model, the droplets are mainly generated at the front of the deformed wave, which
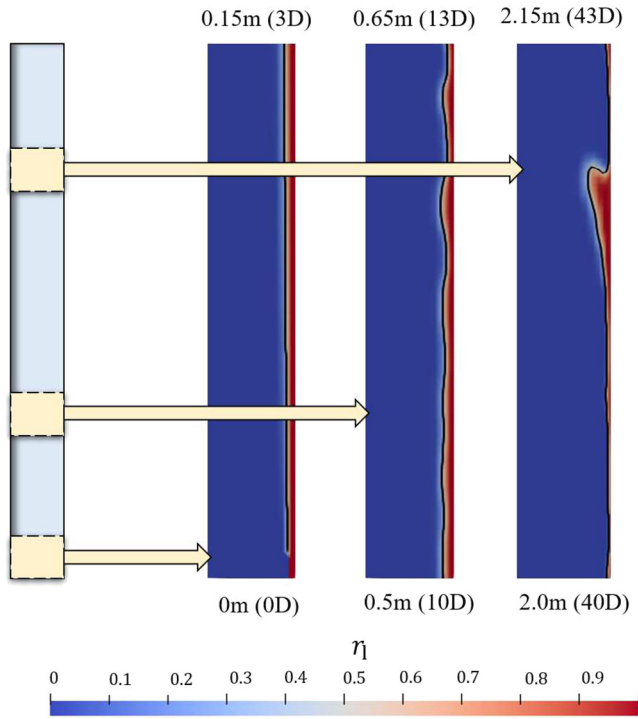
0.15m (3D)   0.65m (13D)   2.15m (43D)

0m (0D)   0.5m (10D)   2.0m (40D)

η_l

0   0.1   0.2   0.3   0.4   0.5   0.6   0.7   0.8   0.9

FIG. 11. Axial development of the interfacial wave.

corresponds to the shear-off effect. However, the droplets in Okawa *et al.*[30] model are generated uniformly at the whole interface, which is independent of the interface shape. Obviously, this is inconsistent with the physical understanding of the entrainment mechanism. In Höhne and Hänsch's model,[35] the entrainment not
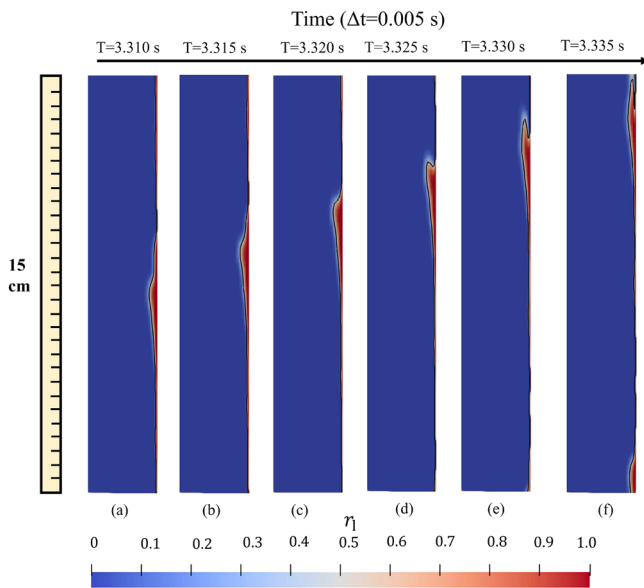

Time (Δt=0.005 s)

T=3.310 s   T=3.315 s   T=3.320 s   T=3.325 s   T=3.330 s   T=3.335 s

15 cm

(a)   (b)   (c)   (d)   (e)   (f)

r_d

0   0.1   0.2   0.3   0.4   0.5   0.6   0.7   0.8   0.9   1.0
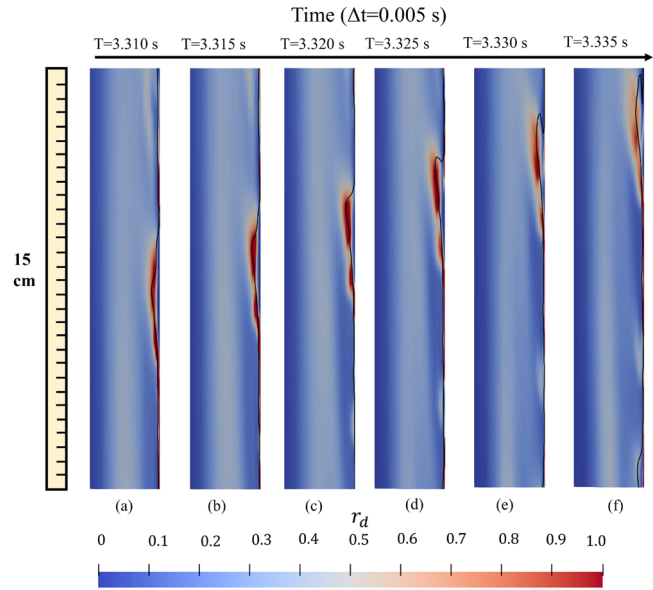
FIG. 13. Generation process of the droplets.

only takes place on the wave tip, but also on the top and the front-bottom of the wave. This could be explained by the turbulent kinetic energy, which is significantly large in these locations.

C. Quantitative results

In this section, quantitative comparison between the simulation and experiment is carried out to evaluate the performance of the proposed entrainment model. The experimental data are from the electrical resistance tomography, which is settled at the location of 3 m. This
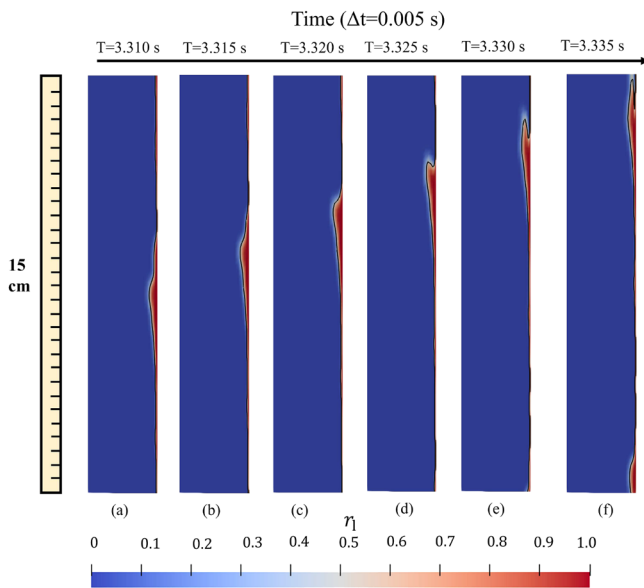

Time (Δt=0.005 s)

T=3.310 s   T=3.315 s   T=3.320 s   T=3.325 s   T=3.330 s   T=3.335 s

15 cm

(a)   (b)   (c)   (d)   (e)   (f)

η_l

0   0.1   0.2   0.3   0.4   0.5   0.6   0.7   0.8   0.9   1.0

FIG. 12. Development of the interfacial wave.

Time (Δt=0.005 s)

T=3.310 s   T=3.315 s   T=3.320 s   T=3.325 s   T=3.330 s   T=3.335 s

15 cm

(a)   (b)   (c)   (d)   (e)   (f)

$-\Gamma_d$ (kg/(m³s))

-500   -450   -400   -350   -300   -250   -200   -150   -100   -50   0

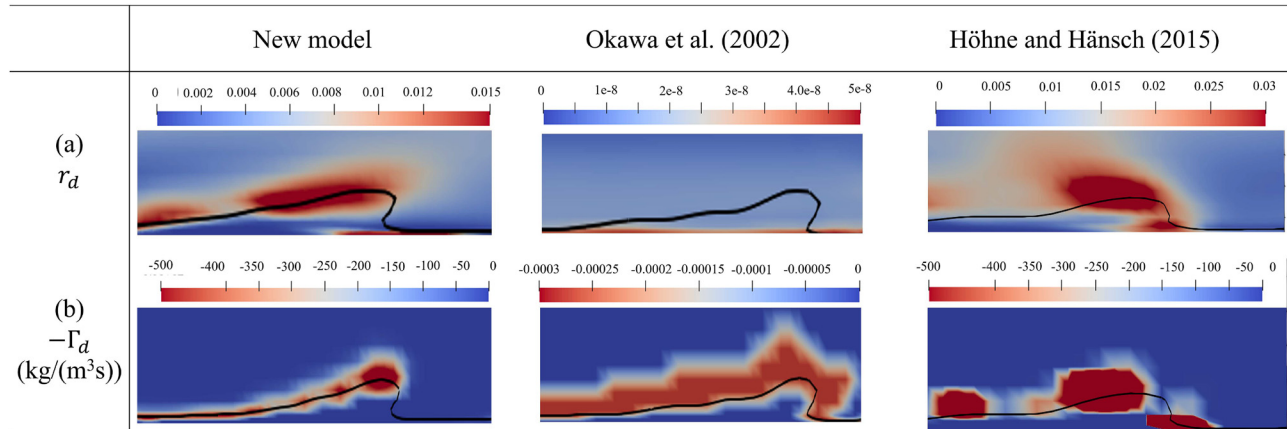**FIG. 14.** Visualization of the entrainment rate.

FIG. 15. Comparisons of liquid film fraction, droplet fraction, and entrainment rate from different models.

position belongs to the fully developed entrainment region. However, as aforementioned, the simulation in this work ignores the droplet deposition, so that using the data in the fully developed region from the simulation could be questionable. A compromise is to use a section that can reflect the fully entrainment feature and minimize the effect of droplet deposition. With this in mind, the following discussion uses the quantitative results from the sample section of $z = 2.0$ m, which is close to the beginning of the fully developed entrainment region.

Figure 16(a) shows the temporal evolution of the liquid film fraction, which is calculated by the cross-sectional integral of the liquid film fraction, r_l. Both the experimental data and the simulation result exhibit oscillatory behavior, and each peak represents an interfacial wave passing the cross section of data acquisition. The order of magnitude of the liquid film fraction oscillations observed in the simulation is comparable to the experimental ones. At the same time, the simulated wave frequency seems to be significantly higher than the measured one. Figures 16(b) and 16(c) compare the time series of film fraction from different entrainment models. It can be seen that the simulated results from the new model and the correlations of Okawa et al.[30] and Höhne and Hänsch[35] show similar magnitude and oscillation amplitude.

In order to further investigate the liquid film fraction, statistical quantities of the time series data from Fig. 16 are calculated, and the results are temporally averaged between 1 and 4 s. For that purpose, the time-averaged value (AVE) of the time series as well as the standard deviation (STD) are graphically presented in Fig. 17. The results show that the void fraction obtained with the new model is slightly larger than the experimental data, while the estimation of Okawa et al.'s[30] model reveals a larger liquid film fraction compared to the experiment. A consequence is that less droplets are estimated by Okawa et al.'s[30] model. The void fraction of Höhne and Hänsch's model[35] is slightly lower than observed in the experimental data, denoting that a higher rate of droplet formation is predicted by their model. The standard deviation implies the oscillation amplitude of the liquid film fraction, and Fig. 17 shows that it is slightly larger in the new model and Okawa et al.'s[30] model compared to the experimental value, while the STD in Höhne and Hänsch's model is smaller. Overall, this justifies the conclusion that the amplitudes of oscillations from simulations and experiment are comparable.

The probability density function (PDF) of the liquid film fraction is another parameter characterizing annular flow. As shown in Fig. 18, all models results in a single peak. The peak of the curve obtained with Okawa et al.'s[30] model is shifted toward larger film fractions compared with the experimental data. The peak of the PDF of liquid film fraction obtained with Höhne and Hänsch's model[35] is significantly more pronounced than observed in the experiment. The new model's PDF curve has almost similar peak position and curve shape compared with the experimental curve, so that the new model agrees well with the experimental data and outperforms Okawa et al.[30] and Höhne and Hänsch's[35] models in this regard. This can be explained by shear-off effect as the underlying mechanism of the proposed model being consistent with the physical entrainment behavior in annular flow. One discrepancy between the simulation and experiment is that the experimental PDF curve is smoother than the simulated one, which could be caused by an insufficient number of data points and averaging time period in the CFD simulations carried out.

To compare the liquid fraction's characteristic in the frequency domain, fast Fourier transform is used to calculate the power spectral density (PSD), as shown in Fig. 19. It is clear that the PSD curves from the experiment and the three models exhibit similar lognormal distribution in frequency space. However, the PSD curve obtained from the three models is shifted toward higher frequencies compared with the experiment. This implies that the characteristic, i.e., maximum, frequency obtained from simulation (around 20 Hz) is multiple times higher than observed in the experiment (around 4 Hz). This is consistent with the observation in Fig. 16, where more frequent peaks are observed in the temporal evolution of the liquid film fraction from the simulation than in the experiment. This could be explained by the interface not being fully resolved in this work, so that the specific wave parameter is not matched on the computational grid. Fully resolving the interface is out of the scope of this work because of extensive requirements of computational resources and might be in the focus of future investigations.
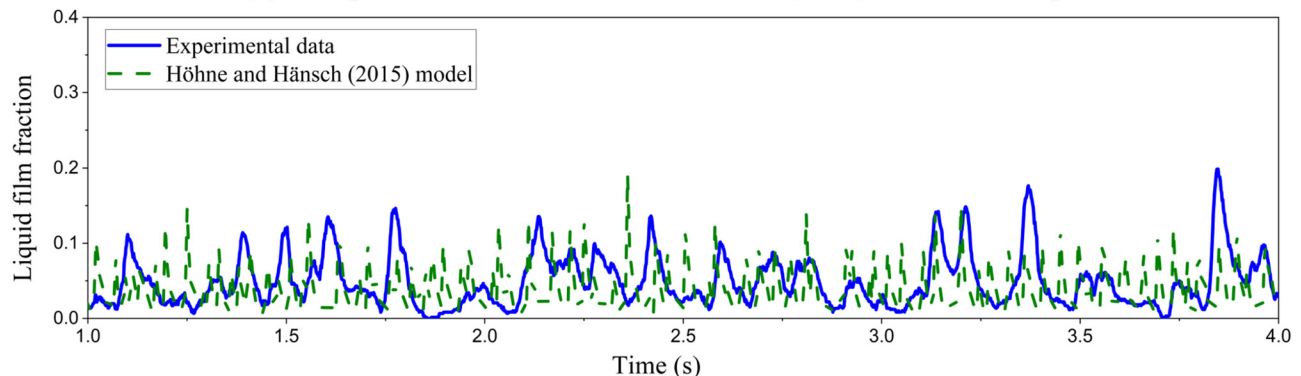
VI. CONCLUSIONS

In order to model the annular flow with the morphology-adaptive multifield two-fluid model *MultiMorph*, a new droplet entrainment model is proposed, which predicts the mass transfer rate
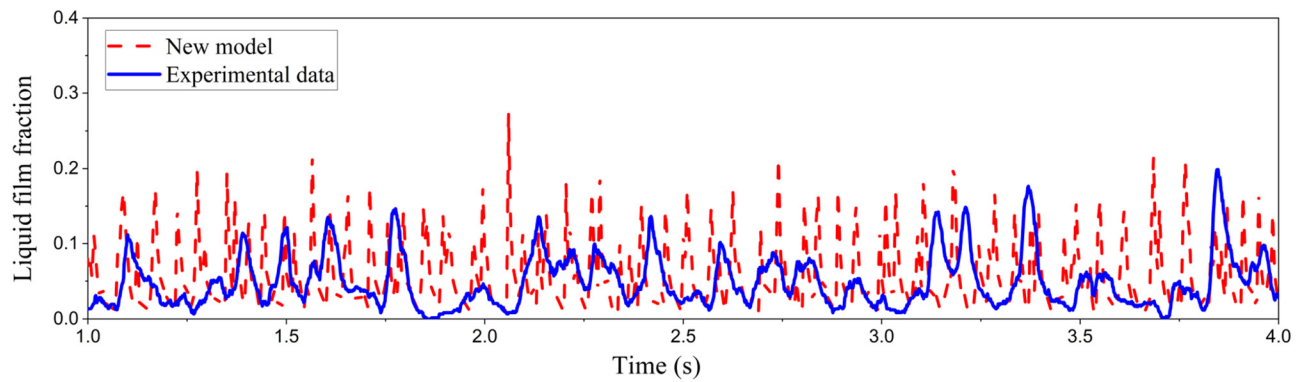
(a) Comparison between the new model and experiment
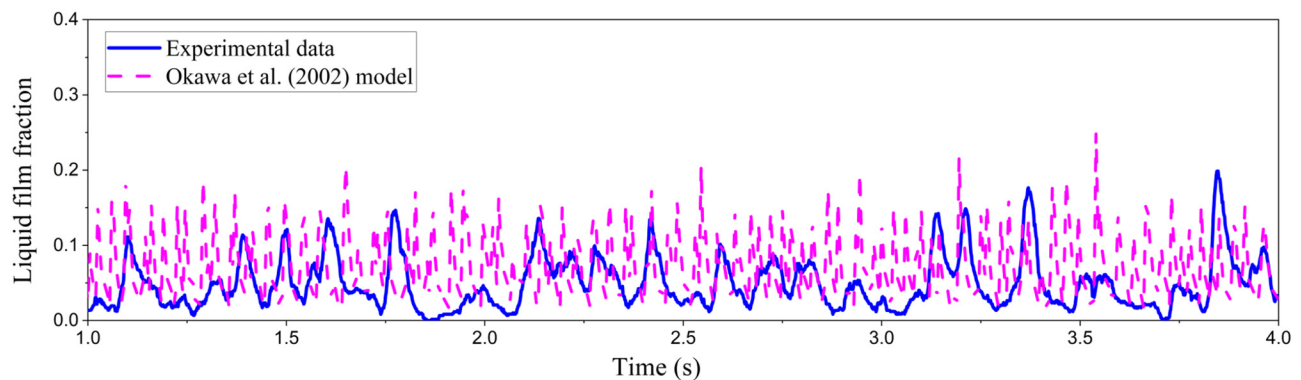
(b) Comparison between the Okawa et al. (2002) model and experiment

(c) Comparison between the Höhne and Hänsch (2015) model and experiment

FIG. 16. Comparisons of time series of liquid film fraction.

from continuous liquid film to dispersed droplets. The new entrainment model is developed having the roll wave mechanism in mind, so that local shear dominates the entrainment process. In contrast to previous entrainment models, the proposed model is based on local parameters in the flow field, which makes it suitable to be applied in CFD codes. The model was implemented into the *MultiMorph* model[26,54] to simulate the three structures in annular flow in a common computational domain. Each structure is represented as a

separate numerical phase: continuous liquid film, continuous gas core, and disperse droplets, where the droplets are generated from the liquid by the proposed model. The simulation results were compared against laboratory experiments and correlations from the literature.

The droplet entrainment rate obtained with the new model compares well with the experiment in the developing entrainment region. Qualitative results show that the proposed entrainment model can predict the interfacial wave and the generation of droplets well.
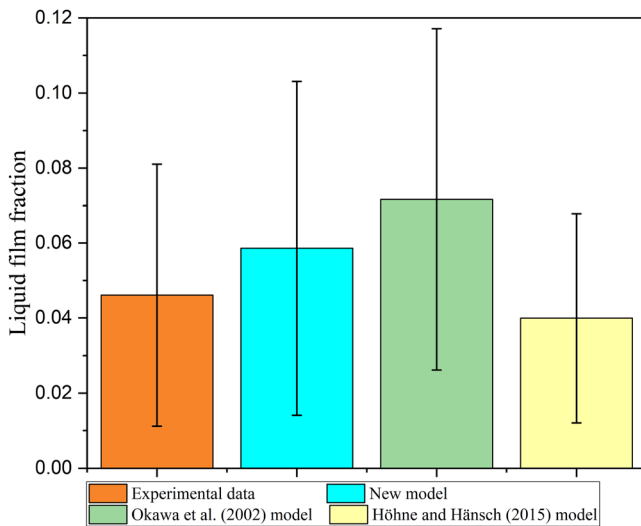
FIG. 17. Comparisons of AVE and STD from different models.

The interfacial wave is generated gradually, from the pipe inlet to large scale waves further downstream, where the shear-off effect is observed. The droplets are generated from the interfacial waves, with the entrainment located mainly at the front tip of the wave. Quantitative results for the liquid film fraction time series data show that the statistical parameters of average value, standard deviation, probability density function, and power spectral density are similar to the experimental data. However, the frequency of the interfacial wave from the simulation is higher than the experiment. Finally, the performance of the proposed model is compared to existing models. The new model exhibits good performance because the generation of the droplets and the droplet fraction from the new model better matches the physical understanding and experimental data compared to the correlations from the literature.
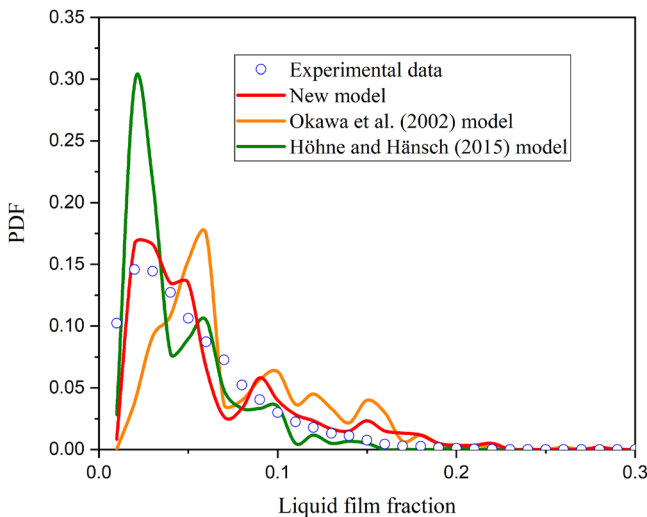

FIG. 18. Comparison of PDF of liquid film fraction predicted by the different entrainment models.[30,35]
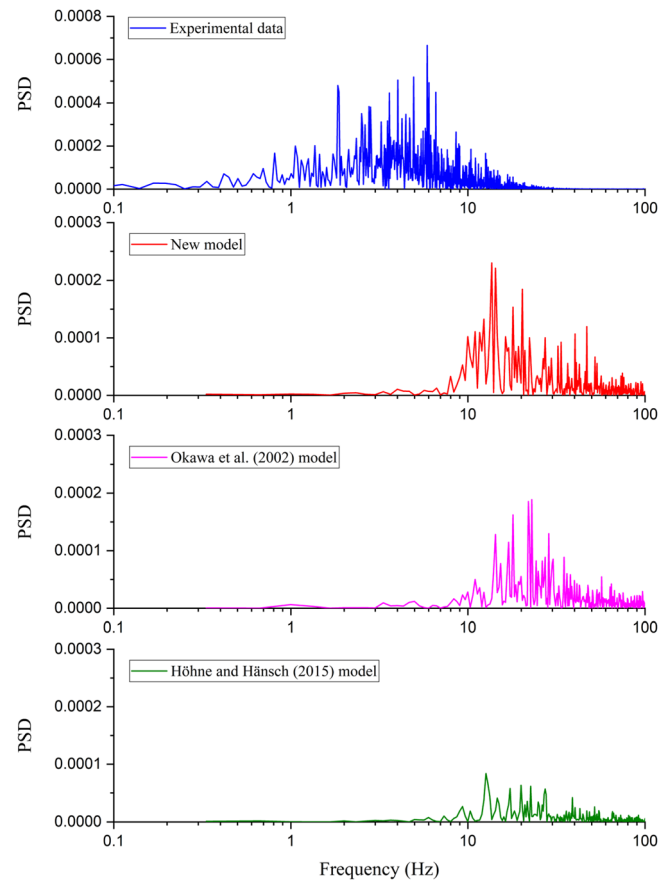

FIG. 19. Comparisons of PSD curves from different models.

Future work is required to improve the modeling of annular flow further. Currently, there is a lack of a reliable deposition model that simulate the mass transfer from droplets to liquid film. To model this effect in combination with the proposed entrainment model would be the next logical step. Is of particular interest that the combined application of deposition and entrainment models results in a realistic equilibrium.

08 April 2024 03:17:13

AUTHOR DECLARATIONS

Conflict of Interest

The authors have no conflicts to disclose.

Author Contributions

Lisong Wang: Conceptualization (equal); Data curation (equal); Investigation (equal); Methodology (equal); Software (equal); Visualization (equal); Writing – original draft (equal). **Benjamin Krull:** Conceptualization (equal); Data curation (equal); Methodology (equal); Software (equal); Supervision (equal); Writing – original draft (equal). **Dirk Lucas:** Funding acquisition (equal); Methodology (equal); Project administration (equal); Supervision (equal). **Richard Meller:** Methodology (equal); Resources (equal); Supervision (equal). **Fabian Schlegel:** Methodology (equal); Project administration (equal); Resources (equal); Supervision (equal). **Matej Tekavčič:** Methodology (equal); Resources (equal). **Jing-Yu Xu:** Funding acquisition (equal); Project administration (equal); Resources (equal); Supervision (equal).

DATA AVAILABILITY

The data that support the findings of this study are available from the corresponding authors upon reasonable request.

NOMENCLATURE

A	Interface indicator field
a_I	Interfacial area density
A_f	Cell face area
C_E	Constant dimensionless parameter in the new entrainment model
C_D	Drag coefficient
d	Droplet diameter
D	Diameter of the pipe
E	Entrainment fraction
$\boldsymbol{F}$	Closure force
F_1	Coefficient of the turbulence model
$\boldsymbol{g}$	Gravitational acceleration
H	Height of the domain
I	Turbulent intensity
k	Turbulent kinetic energy
L_a	Capillary length
L_a	Capillary length scale
$\boldsymbol{M}$	Momentum source term
$\dot{m}_d$	Droplet entrainment rate (area-specific)
N	Number of cells
P	Pressure
$\tilde{P}_\alpha$	Turbulent kinetic energy production term
r	Volume fraction
t	Time
$\boldsymbol{T}$	Effective stress tensor
U	Characteristic velocity
$\boldsymbol{v}$	Velocity
$\boldsymbol{v}^+$	Velocity close to the interface
$\boldsymbol{v}_{\alpha\beta,\text{slip}}$	Slip velocity, $\boldsymbol{v}_\alpha - \boldsymbol{v}_\beta$
W	Mass flow rate
z_{cri}	Critical length of fully developed entrainment

AVE	Average value
PDF	Probability density function
PSD	Power spectral density
Re	Reynolds number
STD	Standard deviation
We_I	Interfacial Weber number
β	Coefficient of the k–ω SST turbulence model
Γ_d	Droplet entrainment rate (volume-specific)
Γ	Source term of mass transfer (volume-specific)
γ	Coefficient of the k–ω SST turbulence model
Δ_f	Neighbor cell distance
Δt	Time step size
δ	Thickness of the water inlet
δ_α	Damping length scale
κ	Interface curvature
μ	Dynamic molecular viscosity
μ^T	Eddy viscosity
ξ	Dimensionless distance
ν	Kinematic viscosity
ρ	Density
$\rho_{\alpha\beta}$	Phase-weighted density, $(\alpha\rho_\alpha + \beta\rho_\beta)/(\alpha + \beta)$
σ	Surface tension coefficient
$\sigma_{\omega 2}$	Coefficient of the k–ω SST turbulence model
σ_ω	Coefficient of the k–ω SST turbulence model
χ	Dimensionless parameter used to calculate entrainment fraction
ω	Specific dissipation
$\lfloor . \rfloor_f$	Cell face interpolation
$\|\nabla r_l\|$	Interfacial area density of continuous liquid interface
$(.)_d$	Related to droplet phase
$(.)_g$	Related to gas phase
$(.)_l$	Related to liquid phase
$(.)_{gl}$	Related to gas and liquid film
$(.)_{sl}$	Superficial liquid velocity
$(.)_{sg}$	Superficial gas velocity
$(.)_{in}, (.)^{in}$	Related to inlet condition
$(.)_\alpha, (.)_\beta$	Phase indices
$(.)'$	Modified quantity

REFERENCES

[1]G. Hewitt, *Annular Two-Phase Flow* (Elsevier, 2013).

[2]W. Fan, H. Li, and H. Anglart, "Numerical investigation of spatial and temporal structure of annular flow with disturbance waves," Int. J. Multiphase Flow **110**, 256–272 (2019).

[3]J. M. Rodriguez, *Numerical Simulation of Two-Phase Annular Flow* (Rensselaer Polytechnic Institute, 2009).

[4]Y. Liu, J. Cui, and W. Li, "A two-phase, two-component model for vertical upward gas–liquid annular flow," Int. J. Heat Fluid Flow **32**, 796–804 (2011).

[5]B. C. Nie, X. Guan, J.-M. Vanden-Broeck, and F. Dias, "Air/water interfacial waves with a droplet at the tip of their crest," Phys. Fluids **35**, 012101 (2023).

[6]H. Han and K. Gabriel, "A numerical study of entrainment mechanism in axisymmetric annular gas-liquid flow," J. Fluids Eng. **129**, 293–301 (2007).

[7]P. Kumar, A. K. Das, and S. K. Mitra, "Physical understanding of gas-liquid annular flow and its transition to dispersed droplets," Phys. Fluids **28**, 072101 (2016).

[8]X.-L. Liu, S.-Q. Hu, Y. Wang, L.-L. Liu, and Y. Zhang, "Numerical investigation on the droplet entrainment from gas sheared liquid film of hydroxyl-terminated polybutadiene/paraffin fuels," Phys. Fluids **35**, 012108 (2023).

[9]C.-W. Kuo and M. F. Trujillo, "Simulation of liquid jet atomization and droplet breakup via a volume-of-fluid Lagrangian-Eulerian strategy," Phys. Fluids **34**, 113326 (2022).

[10]Z. Xie, G. F. Hewitt, D. Pavlidis, P. Salinas, C. C. Pain, and O. K. Matar, "Numerical study of three-dimensional droplet impact on a flowing liquid film in annular two-phase flow," Chem. Eng. Sci. **166**, 303–312 (2017).

[11]E. Abobaker, A. Elsanoose, J. Shirokoff, and M. A. Rahman, "Cfd simulation of two-phase vertical annular flow in both upward and downward direction in a small pipe," in *International Conference on Offshore Mechanics and Arctic Engineering* (American Society of Mechanical Engineers, 2019), Vol. 58875.

[12]A. Saxena and H.-M. Prasser, "A study of two-phase annular flow using unsteady numerical computations," Int. J. Multiphase Flow **126**, 103037 (2020).

[13]J. Huo, L. Wang, J. Tang, and X. Shi, "Droplets impact against the random rough surface with a liquid film," Phys. Fluids **35**, 063314 (2023).

[14]S.-J. Wang, Z.-H. Shi, T.-L. Yao, W.-F. Li, and Q.-G. Lin, "Experimental and numerical study of liquid film by jet impingement: Based on contact angle model," Phys. Fluids **35**, 085104 (2023).

[15]D. Caraghiaur and H. Anglart, "Drop deposition in annular two-phase flow calculated with lagrangian particle tracking," Nucl. Eng. Des. **265**, 856–866 (2013).

[16]G. Yun, Y. Ishiwatari, S. Ikejiri, and Y. Oka, "Numerical analysis of the onset of droplet entrainment in annular two-phase flow by hybrid method," Ann. Nucl. Energy **37**, 230–240 (2010).

[17]H. Xie, S. Koshizuka, and Y. Oka, "Numerical simulation of liquid drop deposition in annular-mist flow regime of boiling water reactor," J. Nucl. Sci. Technol. **41**, 569–578 (2004).

[18]S. Wang, H. Wang, Y. Wu, and Y. Cheng, "Numerical simulation of the droplet formation involving fluids with high viscosity ratio by lattice Boltzmann method," Phys. Fluids **35**, 063107 (2023).

[19]Y. Liu and W. Li, "Numerical simulation of droplet size distribution in vertical upward annular flow," J. Fluids Eng. **132**, 121402 (2010).

[20]D. Adechy and R. Issa, "Modelling of annular flow through pipes and t-junctions," Comput. Fluids **33**, 289–313 (2004).

[21]V. Alipchenkov, R. Nigmatulin, S. Soloviev, O. Stonik, L. Zaichik, and Y. Zeigarnik, "A three-fluid model of two-phase dispersed-annular flow," Int. J. Heat Mass Transfer **47**, 5323–5338 (2004).

[22]T. Höhne, T. Geissler, A. Bieberle, and U. Hampel, "Numerical modeling of a horizontal annular flow experiment using a droplet entrainment model," Ann. Nucl. Energy **77**, 351–360 (2015).

[23]H. Li and H. Anglart, "Cfd model of diabatic annular two-phase flow using the eulerian–lagrangian approach," Ann. Nucl. Energy **77**, 415–424 (2015).

[24]H. Li and H. Anglart, "Modeling of annular two-phase flow using a unified cfd approach," Nucl. Eng. Des. **303**, 17–24 (2016).

[25]R. Meller, F. Schlegel, and D. Lucas, "Basic verification of a numerical framework applied to a morphology adaptive multifield two-fluid model considering bubble motions," Int. J. Numer. Methods Fluids **93**, 748–773 (2021).

[26]F. Schlegel, R. Meller, B. Krull, R. Lehnig, and M. Tekavčič, "Openfoam-hybrid: A morphology adaptive multifield two-fluid model," Nucl. Sci. Eng. **197**, 2620–2633 (2023).

[27]A. Cubero, A. Sánchez-Insa, and N. Fueyo, "A consistent momentum interpolation method for steady and unsteady multiphase flows," Comput. Chem. Eng. **62**, 96–107 (2014).

[28]D. B. Spalding, "Numerical computation of multi-phase fluid flow and heat transfer," in *Von Karman Institute for Fluid Dynamics Numerical Computation of Multi-Phase Flows* (1981), pp. 161–191, see https://ui.adsabs.harvard.edu/abs/1981ncmp.vkif..161S/abstract

[29]M. Tekavčič, R. Meller, and F. Schlegel, "Validation of a morphology adaptive multi-field two-fluid model considering counter-current stratified flow with interfacial turbulence damping," Nucl. Eng. Des. **379**, 111223 (2021).

[30]T. Okawa, T. Kitahara, K. Yoshida, T. Matsumoto, and I. Kataoka, "New entrainment rate correlation in annular two-phase flow applicable to wide range of flow condition," Int. J. Heat Mass Transfer **45**, 87–98 (2002).

[31]L. Liu and B. Bai, "Generalization of droplet entrainment rate correlation for annular flow considering disturbance wave properties," Chem. Eng. Sci. **164**, 279–291 (2017).

[32]G. Wang, P. Sawant, and M. Ishii, "A new entrainment rate model for annular two-phase flow," Int. J. Multiphase Flow **124**, 103185 (2020).

[33]M. Holowach, L. Hochreiter, and F. Cheung, "A model for droplet entrainment in heated annular flow," Int. J. Heat Fluid Flow **23**, 807–822 (2002).

[34]I. Kataoka, M. Ishii, and A. Nakayama, "Entrainment and desposition rates of droplets in annular two-phase flow," Int. J. Heat Mass Transfer **43**, 1573–1589 (2000).

[35]T. Höhne and S. Hänsch, "A droplet entrainment model for horizontal segregated flows," Nucl. Eng. Des. **286**, 18–26 (2015).

[36]J. Ma, A. A. Oberai, D. A. Drew, R. T. Lahey, Jr., and M. C. Hyman, "A comprehensive sub-grid air entrainment model for rans modeling of free-surface bubbly flows," J. Comput. Multiphase Flows **3**, 41–56 (2011).

[37]M. Ishii and M. Grolmes, "Inception criteria for droplet entrainment in two-phase concurrent film flow," AIChE J. **21**, 308–318 (1975).

[38]C. Berna, A. Escrivá, J. Muñoz-Cobo, and L. Herranz, "Review of droplet entrainment in annular flow: Characterization of the entrained droplets," Prog. Nucl. Energy **79**, 64–86 (2015).

[39]C. Inoue and I. Maeda, "On the droplet entrainment from gas-sheared liquid film," Phys. Fluids **33**, 011705 (2021).

[40]J. U. Brackbill, D. B. Kothe, and C. Zemach, "A continuum method for modeling surface tension," J. Comput. Phys. **100**, 335–354 (1992).

[41]M. Ishii and K. Mishima, "Two-fluid model and hydrodynamic constitutive relations," Nucl. Eng. Des. **82**, 107–126 (1984).

[42]F. R. Menter, "Two-equation eddy-viscosity turbulence models for engineering applications," AIAA J. **32**, 1598–1605 (1994).

[43]E. Frederix, A. Mathur, D. Dovizio, B. Geurts, and E. Komen, "Reynolds-averaged modeling of turbulence damping near a large-scale interface in two-phase flow," Nucl. Eng. Des. **333**, 122–130 (2018).

[44]G. Agostinelli, "Advancement of closure relations for annular flow modeling in CFD," Ph.D. thesis (Massachusetts Institute of Technology, 2020).

[45]L. Schiller and A. Naumann, "A drag coefficient correlation," Zeit. Ver. Deutsch. Ing. **77**, 318–320 (1933).

[46]R. Meller, M. Tekavčič, B. Krull, and F. Schlegel, "Momentum exchange modelling for coarsely resolved interfaces in a multifield two-fluid model," Int. J. Numer. Methods Fluids **95**, 1521–1545 (2023).

[47]J. Xie, L. Liu, X. Huo, X. Liu, and R. Duan, "Numerical and experimental study of wire mesh in the swirl effervescent atomization," Phys. Fluids **35**, 082110 (2023).

[48]S. Liu, J. Zhang, and J.-Y. Xu, "An investigation of a gas–liquid swirling flow with shear-thinning power-law liquids," Phys. Fluids **34**, 073320 (2022).

[49]J. Jia, M. Wang, H. Schlaberg, and H. Li, "A novel tomographic sensing system for high electrically conductive multiphase flow measurement," Flow Meas. Instrum. **21**, 184–190 (2010).

[50]I. Kataoka and M. Ishii, "Mechanism and correlation of droplet entrainment and deposition in annular two-phase flow. [PWR; BWR]," Technical Report No. NUREG/CR-2885 (Argonne National Laboratory, IL 1982).

[51]A. M. Aliyu, A. A. Almabrok, Y. D. Baba, A.-E. Archibong, L. Lao, H. Yeung, and K. C. Kim, "Prediction of entrained droplet fraction in co-current annular gas–liquid flow in vertical pipes," Exp. Therm. Fluid Sci. **85**, 287–304 (2017).

[52]S. Alekseenko, V. Antipin, A. Cherdantsev, S. Kharlamov, and D. Markovich, "Two-wave structure of liquid film and wave interrelation in annular gas-liquid flow with and without entrainment," Phys. Fluids **21**, 061701 (2009).

[53]S. V. Alekseenko, A. V. Cherdantsev, O. M. Heinz, S. M. Kharlamov, and D. M. Markovich, "Analysis of spatial and temporal evolution of disturbance waves and ripples in annular gas–liquid flow," Int. J. Multiphase Flow **67**, 122–134 (2014).

[54]F. Schlegel, K. G. Bilde, M. Draw, I. Evdokimov, S. Hänsch, "V. V. Kamble, H. Khan, B. Krull, R. Lehnig, J. Li, H. Lyu, R. Meller, G. Petelin, S. P. Kota, and M. Tekavčič, Multiphase code repository by HZDR for OpenFOAM foundation software" (2023), see https://www.hzdr.de/db/!Publications?pNid=head&pSelMenu=0&pSelTitle=32194.